aerospace

MDPI

Article

Effect of Nose Bluntness on Boundary-Layer Transition of a Fin–Cone Configuration at Mach 6

Ziyan Fang [1], Lang Xu [1], Duolong Xu [1], Xueliang Li [1], Fu Zhang [2] and Jie Wu [1,3,*]

[1] Department of Engineering Mechanics, School of Aerospace Engineering, Huazhong University of Science and Technology, Wuhan 430074, China; fangziyan2022@163.com (Z.F.); m202472097@hust.edu.cn (L.X.); m202472107@hust.edu.cn (D.X.); xueliang_li@163.com (X.L.)
[2] Beijing Institute of Aerospace Long March Vehicle, Beijing 100076, China; zfu@mail.ustc.edu.cn
[3] Hubei Key Laboratory of Engineering Structural Analysis and Safety Assessment, Huazhong University of Science and Technology, Wuhan 430074, China
* Correspondence: jiewu@hust.edu.cn

Abstract

Experiments on hypersonic boundary-layer instability of a fin–cone configuration were conducted in a Φ 0.5 m Mach 6 Ludwieg tube tunnel. Infrared thermography and high-frequency pressure sensors were used to measure the transition front and instability waves under four different nose bluntness conditions. On the leeward surface, transition is delayed near the centerline due to expansion waves generated by the double-cone structure. The region close to the corner is strongly influenced by the horseshoe vortex, whereas instability waves around 110 kHz manifest as the flow moves away from it. In contrast, transition on the windward surface occurs earlier and broadband high-frequency instability waves of 160–300 kHz are present near the corner. Increasing nose bluntness strongly suppresses transition away from the fin root, especially near the centerline and on the fin-off cone side, but has a relatively limited impact on the shock-interaction regions near the fin–cone corner. Transition on the fin surface remains insensitive to nose bluntness variations. This work elucidates the distinct transition behaviors across different regions of a complex fin–cone configuration and their differential responses to nose bluntness, providing valuable insights for the aerodynamic design and transition prediction of hypersonic vehicles.

Keywords: hypersonic flow; boundary-layer transition; fin–cone configuration; nose bluntness; instability waves

1. Introduction

Hypersonic boundary-layer transition is one of the paramount challenges in the field of aerodynamics. The evolution of boundary layer flow from laminar to turbulent leads to a significant increase in both skin friction drag and heat flux on the vehicle surface, thereby posing a formidable challenge for the design of thermal protection systems and aerodynamic configurations [1].

Hypersonic vehicles typically employ complex topological configurations to meet the requirements of multi-mission capability, high maneuverability, and wide-speed-range flight. Existing research has predominantly focused on simple geometries such as sharp cones or flat plates, spherically blunted cones, hypersonic forebodies, and flat-plate delta wings, where the instability modes are relatively isolated and thus difficult to reflect the complex transition characteristics of real vehicles [2]. In particular, research on highly

Check for updates

Academic Editor: Kung-Ming Chung

Received: 12 November 2025
Revised: 25 December 2025
Accepted: 29 December 2025
Published: 8 January 2026

Copyright: © 2026 by the authors. Licensee MDPI, Basel, Switzerland. This article is an open access article distributed under the terms and conditions of the Creative Commons Attribution (CC BY) license.

swept fin–cone configurations remains relatively scarce. The boundary layer of such configurations exhibits simultaneous instabilities of Mack mode instability, crossflow instability, and vortex instability, which leads to complex transition mechanisms and significant challenges in numerical prediction. Therefore, urgent and in-depth investigations into this topic are imperative.

To address this research gap, the Office of Naval Research has recently funded an investigation into boundary-layer transition for conical bodies with highly swept fins [3]. Using Direct Numerical Simulation (DNS), Knutson et al. identified two steady vortex systems: the horseshoe vortex system on the cone and the leading-edge vortex system on the fin. Additionally, the study found that significant crossflow exists on both the cone and the fin surfaces [4]. Furthermore, by introducing small-amplitude perturbations into the base flow, they uncovered two typical instability mechanisms: the Mack second-mode and a newly identified horseshoe vortex instability localized in high-gradient regions [5]. Mullen used Linear Parabolized Stability Equations to systematically investigate the influence of key geometric parameters on the surface heat flux distribution, revealing that the second-mode is the dominant instability mechanism for this configuration [6,7]. However, the studies by Knutson and Mullen are limited to the analysis of linear low-amplitude disturbances, thus falling short of replicating real-world conditions [5,6]. Meanwhile, Turbeville and Schneider conducted supporting experimental studies in the Boeing/AFOSR Mach-6 Quiet Tunnel (BAM6QT) at Purdue University. They demonstrated that transition on the cone surface was delayed by increasing the sweep angle, decreasing the fin leading-edge bluntness, and increasing the nose radius [8]. Furthermore, they innovatively adopted a rotating model to obtain refined pressure fluctuation measurements at multiple azimuthal angles, capturing both high-frequency second-mode and low-frequency instabilities on the cone surface. By combining this approach with infrared (IR) thermography, they successfully isolated the heat flux contributions from the base flow and the transition process [9]. On this basis, Turbeville et al. systematically investigated the effect of nose bluntness on boundary-layer transition, finding that increased nose bluntness can delay transition but has no significant impact on the frequency characteristics or amplitude of the instability. Spectral analysis further suggested a potential inverse relationship between instability frequency and vortex diameter, indicating that vortex-induced instability may dominate the transition process [9,10]. Araya applied multiple linear stability methods to confirm a strong correlation between high-frequency vortex instability and the transition onset observed in BAM6QT experiments [11]. Middlebrooks carried out wind tunnel tests in a Mach 6 Ludwieg tube, revealing that increasing nose bluntness can suppress the development of horseshoe vortices on the cone surface but enhance the primary vortex on the fin [12].

Although the fin–cone configuration has received a certain amount of interest, many aspects of its transition mechanism remain unclear, especially under the condition of asymmetric upper and lower surfaces, where the flow characteristics become more complex. To address these issues, this study designed a complex fin–cone configuration, which consists of a single-sided swept delta fin and a non-axisymmetric cone, and arranged a high-density sensor array on the model surface. This paper first introduces the experimental facility, experimental model, and testing techniques. Subsequently, a high-speed IR thermal camera was used to monitor the temperature on the model surface, enabling the acquisition of the temperature-rise distribution of the fin–cone model before and after each wind-tunnel run. Simultaneously, PCB high-frequency pressure sensors were used to measure the surface pressure fluctuations on the cone and fin surface, providing detailed information on the evolution of instability waves. This work investigates the flow characteristics and boundary-layer instability mechanisms of the fin–cone configuration in hypersonic wind

tunnels with particular emphasis on assessing the effect of nose bluntness on boundary-layer transition in the complex fin–cone configuration.

2. Experimental Setup

2.1. Facility and Experimental Conditions

This experiment was conducted in the Φ 0.5 m Mach 6 Ludwieg tube tunnel at Huazhong University of Science and Technology (HUST), as shown in Figure 1. This facility is mainly composed of a double-bend gas storage tube, an upstream quick-opening valve, a Laval nozzle, a test section, a diffuser section, and a vacuum tank. The wind tunnel has an effective test duration of over 100 ms, with a test section exit diameter of 0.5 m and a maximum operating total temperature of 600 K, enabling a maximum unit Reynolds number of 3.00×10^7 m^{-1}. When the freestream unit Reynolds number ranges from 4.31×10^6 m^{-1} to 1.08×10^7 m^{-1}, the normalized Pitot pressure fluctuation in the test section decreases from 1.5% to 0.7% [13]. This Ludwieg tube tunnel exhibits good experimental repeatability, which has been confirmed by the team's prior related studies [14]. Table 1 summarizes the experimental freestream conditions. The parameters include freestream Mach number Ma, total temperature T_0 and total pressure P_0 in the gas storage tube, static temperature T and static pressure P of the freestream, and freestream unit Reynolds number Re_∞.

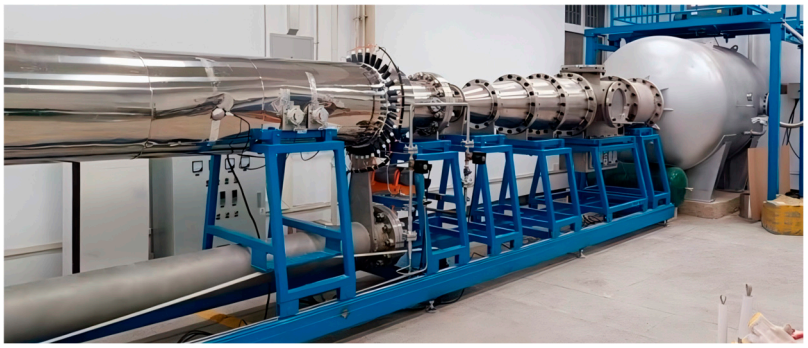


Figure 1. HUST Φ 0.5 m Mach 6 Ludwieg tube tunnel.

Table 1. Experimental freestream conditions.

Ma	T_0 (K)	P_0 (pa)	T (K)	P (pa)	Re_∞ (m^{-1})
6	400.00	5.00×10^5	48.78	253.34	6.09×10^6
6	400.00	1.10×10^6	48.78	696.70	1.34×10^7
6	400.00	1.40×10^6	48.78	886.70	1.70×10^7

2.2. Model

The geometric dimensions of the fin–cone model are shown in Figure 2. The model consists of a single-sided swept delta fin and a non-axisymmetric cone, with an overall length of 452.34 mm and a nose radius of R_n = 2.34 mm. The fin is located on the right side of the cone; it has a fin sweep angle of 75°, with the fin root leading edge 99.57 mm away from the cone nose, and the half-span width of the swept fin at the model base is 61.92 mm. An inflection point is located on the upper surface, 189.84 mm from the nose, which is designed to generate expansion waves; the half-cone angles of the two cone segments before and after the inflection point are 7.3° and 4°, respectively, while the lower surface has a half-cone angle of 2.7°. It is worth noting that all experiments were conducted at zero angle of attack, where the upper surface is defined as the leeward side and the lower surface as the windward side. A coordinate system was established with the nose (for the

case of R_n = 2.34 mm) as the origin. The model centerline is defined along the central axis of the sharp cone. The *X*-axis is aligned with the freestream direction (positive downstream), the *Y*-axis is oriented spanwise along the cone surface (positive toward the fin) and the *Z*-axis completes the right-handed system.

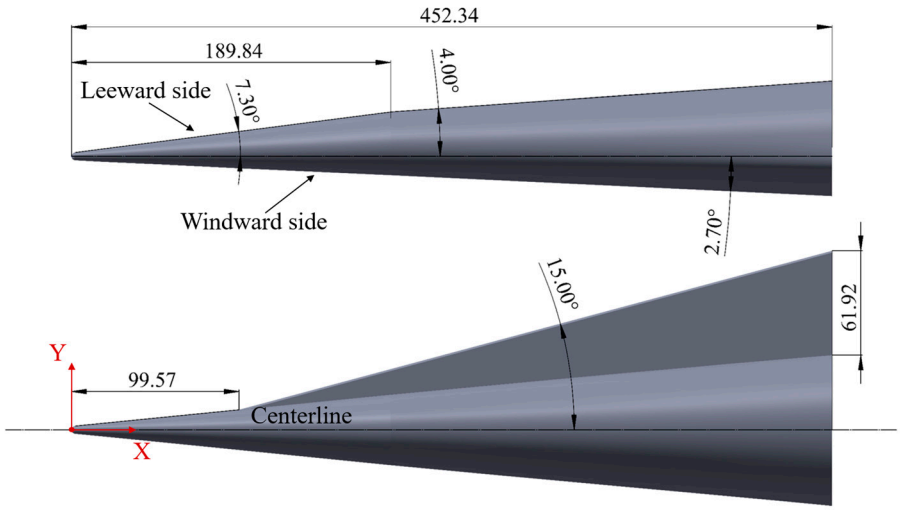
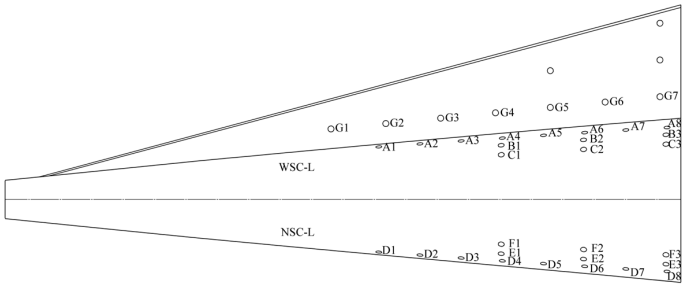
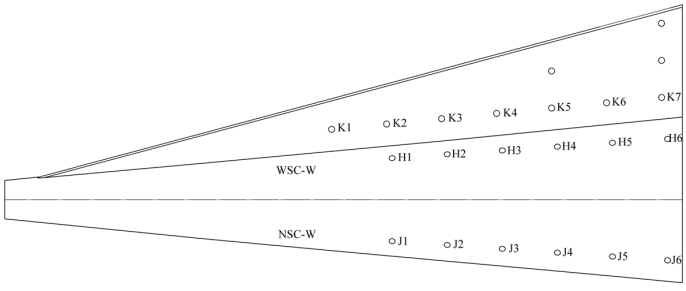


Figure 2. Dimensions of the fin–cone model.

To fully investigate the evolution of instability waves, an array of PCB sensor holes was densely placed on the leeward and windward sides near the fin–cone corner and on the fin surface of the model. Meanwhile, corresponding sensor holes were also arranged on the cone surface without the fin to facilitate comparison. A schematic diagram of the sensor layout is shown in Figure 3, and their specific positions are included in Appendix A. For the convenience of subsequent description, the cone region with the fin attached is defined as the Wing Side Cone (WSC), while the fin-off side of the cone is defined as the Non-wing Side Cone (NSC). Additionally, the leeward and windward sides are distinguished by the suffixes "-L" and "-W", respectively.



(**a**)



(**b**)

Figure 3. Sensor layout of the fin–cone model: (**a**) leeward side; (**b**) windward side.

The physical assembly drawing of the fin–cone model is shown in Figure 4. The model comprises four parts: nose, fin–cone body, connecting rod, and base. Among these, the nose, connecting rod, and base are all made of 304 stainless steel and are detachable. The cone body and fin are integrated as a single unit, constructed from PEEK material. The surface roughness of the model is Ra 3.2. For investigating the effects of nose bluntness, four different nose radii, R_n = 0.06 mm, R_n = 0.56 mm, R_n = 1.125 mm, and R_n = 2.34 mm, were designed for replacement, as shown in Figure 5.

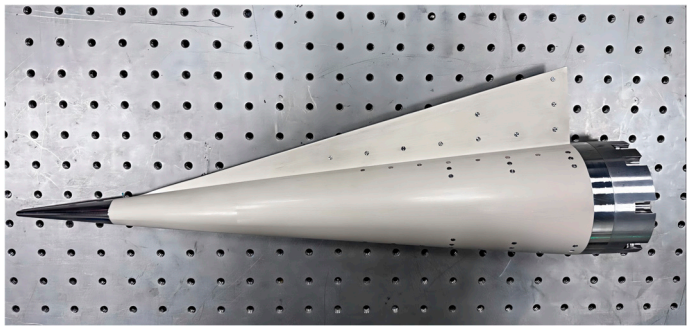


Figure 4. Physical assembly of the fin–cone model.

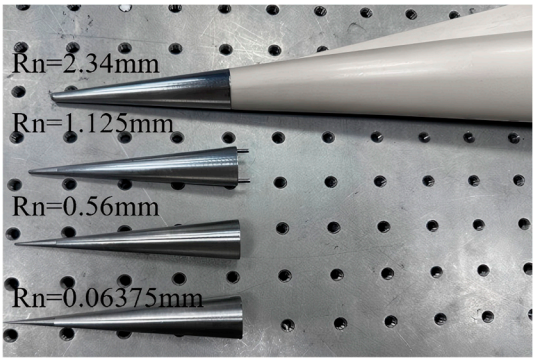


Figure 5. Four different nose radii.

2.3. Test Techniques and Data Analysis

The IR thermography measurements are performed using IRMC-615BB system (IRSV, Beijing, China). This device has a temperature resolution of less than 20 mK, a frame rate of 200 Hz, and a pixel resolution of 640 × 512. When the flow transitions from laminar to turbulent, the convective heat transfer coefficient increases sharply, leading to a rapid rise in the model surface temperature. This abrupt temperature change serves as a key criterion for determining the boundary-layer transition location. By calculating the difference between IR images captured before and after the wind tunnel operation, the model surface temperature rise (ΔT) can be obtained. A calcium fluoride IR viewing window was used in the experiment to meet the requirements of optical measurements.

On the model surface, the sensors are installed in a flush-mounted manner. The high-frequency pressure sensor used is model PCB132B38 (PCB Piezotronics, Inc., Buffalo, NY, USA), which has a pressure measurement resolution of 7 Pa, an effective dynamic response range of 10–1000 kHz, a natural frequency above 1 MHz, and the advantage of high-pass filtering characteristics [15–18]. During the experiment, the sampling frequency was set to 3 MHz, and the acquisition time was set to 1 s. For the signals collected by the PCB sensor, Power Spectral Density (PSD) analysis was performed: the effective signal length was selected as 40 ms, a Hamming window with 50% overlap was used for windowing, and each window contained 2048 sampling points.

To evaluate the statistical reliability of the PSD characteristics, an uncertainty quantification was performed on the pressure fluctuation data. For each wind tunnel run, the effective data segment was divided into three independent 40 ms sub-segments, and the PSD was computed individually for each. This provides a statistical sample of PSDs under identical flow conditions. All PSD curves presented in Section 4 represent the average PSD obtained from all sub-segments. To visualize the statistical variability, Figure 6 shows, as an example, the results from PCB A1–A8 under the condition R_n = 0.06 mm, $Re_\infty = 6.09 \times 10^6$ m^{-1}. The figure displays the average PSD (solid line) along with a statistical ±1 standard error band (shaded region). This band quantifies the inherent random uncertainty in the PSD estimation, which arises from the finite data length under the given experimental conditions. The PSD analysis in Section 4 demonstrates that the systematic changes in PSD induced by variations in nose bluntness are substantially larger in magnitude than the width of the statistical variability band shown in Figure 6. Consequently, the spectral evolution trends revealed through PSD comparisons in this work possess statistical significance and can be attributed to the physical alteration of the nose bluntness parameter, rather than to random measurement fluctuations.

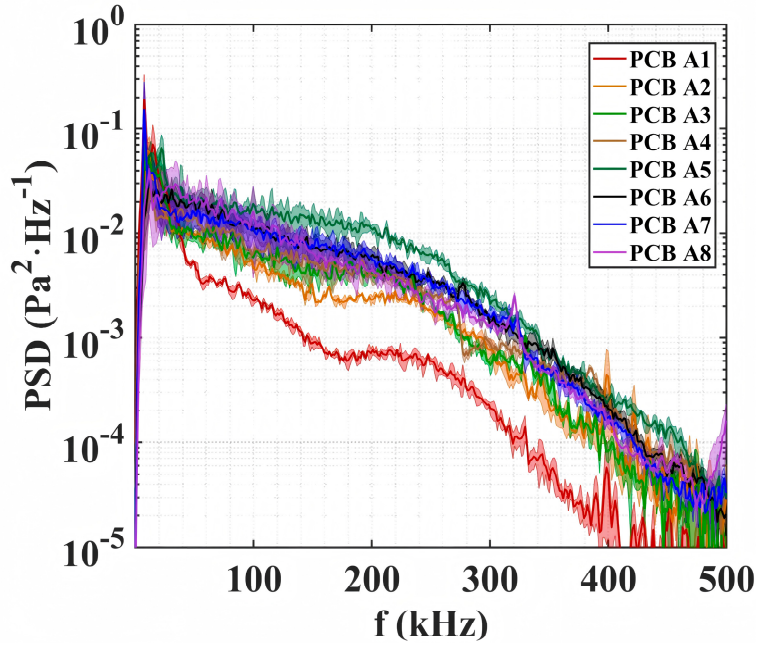


Figure 6. Average PSD with ±1 standard error band for PCB A1–A8, R_n = 0.06 mm, $Re_\infty = 6.09 \times 10^6$ m^{-1}.

In addition, the Continuous Wavelet Transform (CWT) analysis method was applied to process the pressure fluctuation signals acquired by the PCB sensor. The Morse wavelet was selected as the mother wavelet, and the effective operation time was truncated to 2 ms.

3. Surface Thermal Characteristic Analysis

3.1. Leeward Side

Figure 7 presents the IR thermographic images of the fin–cone model's leeward surface under four different nose bluntness conditions, with a freestream Reynolds number of $Re_\infty = 6.09 \times 10^6$ m^{-1}. The images exhibit typical heat flux characteristics of this geometric configuration. Influenced by the bow shock wave, the heat flux at the fin leading edge is the highest. Two heat flux streaks (streak 1 and streak 2) are observed on the cone. The primary heating streak (streak 1) is located in very close proximity to the fin–cone corner, which serves as strong evidence for the presence of horseshoe vortices. This is a typical flow structure induced when hypersonic flow passes over protuberances such as

blunt fins [19], and its intensity gradually decays along the streamwise direction [4]. The downward displacement of the boundary layer by the horseshoe vortex leads to a local thinning and compression of the boundary layer, which enhances wall-normal temperature gradients and results in elevated surface heat flux [20]. The secondary streak (streak 2) is located in a more outward region, with a heat flux density lower than that of the primary streak; it extends almost from the fin root leading edge to the aft end of the model and spreads in the aft end region. These streaks suggest a secondary vortex system formed by secondary separations, which is consistent with the structures observed by Middlebrooks under noisy flow experimental conditions [8,12]. A triangular heating feature is observed near the corner region. Based on subsequent PCB measurements presented in Section 4, it is known that the flow near the corner is at least transitional, and in some areas even fully turbulent. Thus, this heating feature is caused by the combined effect of the base flow vortex structures and the boundary-layer transition here. Away from the corner, near the centerline of the cone's leeward surface and in the NSC-L region, the heat flux is relatively low, and the flow remains mostly laminar. This phenomenon is attributed to the fact that the transition near the centerline of the model's leeward surface is dominated primarily by the second mode, while the expansion waves generated by the inflection point located at X = 189.84 mm upstream suppress the growth of this mode. Li et al. have verified this mechanism under similar freestream conditions [2]. The heating features on the model's fin surface are mainly caused by boundary-layer transition. The transition front is parallel to the fin leading edge.

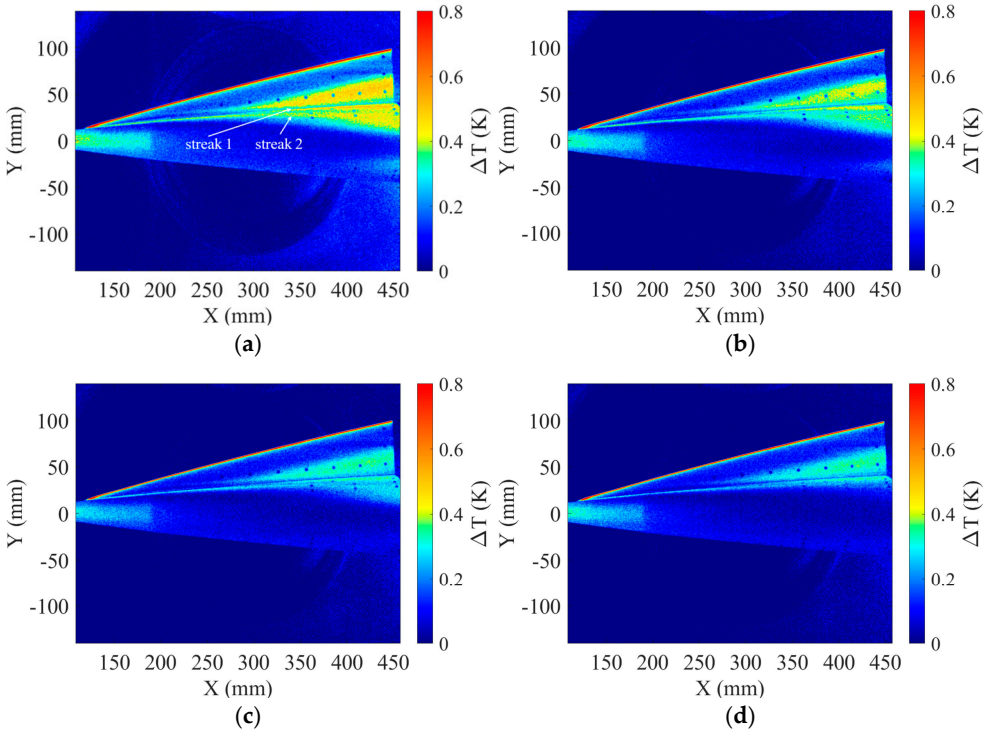


Figure 7. IR images of the leeward surface, $Re_\infty = 6.09 \times 10^6$ m^{-1}: (**a**) R_n = 0.06 mm; (**b**) R_n = 0.56 mm; (**c**) R_n = 1.125 mm; (**d**) R_n = 2.34 mm.

At R_n = 0.06 mm, two heat streaks formed by horseshoe vortices are clearly visible in the WSC-L region, with a large spread range on the cone. At this point, boundary-layer transition occurs in the NSC-L region, and its initial transition location is at X ≈ 380 mm. At R_n = 0.56 mm, the heating range on the cone decreases, and the initial transition location of the NSC-L region is delayed to X ≈ 400 mm. When the nose bluntness radius is reduced to R_n = 1.125 mm and R_n = 2.34 mm, the heating features in the WSC-L re-

gion further diminish, while the NSC-L region remains in a fully laminar state. At these Reynolds numbers, an increase in nose bluntness appears to reduce the distance between the two streaks in the WSC-L region, suppressing the development of horseshoe vortices and significantly narrowing the heating range. In the NSC-L region, an increase in nose bluntness leads to a delay in boundary-layer transition. However, on the fin surface, the position of the transition front relative to the leading edge seems consistent across all nose bluntness conditions.

When the freestream Reynolds number increases to $Re_\infty = 1.70 \times 10^7$ m^{-1}, as shown in Figure 8, the heat flux on the fin and cone of the leeward surface increases significantly. The heat streaks formed by horseshoe vortices on the cone become more distinct, the distance between the two streaks increases, and the heating region shifts substantially upstream with an expanded coverage area. At this point, except for the case with $R_n = 2.34$ mm, transition occurs near the centerline of the leeward surface, and the overall transition front exhibits a "V"-shaped distribution. At this Reynolds number, with the increase in nose bluntness, the "V"-shaped transition front shifts noticeably downstream. For $R_n = 2.34$ mm, the cone surface remains mostly laminar except for the region near the corner. Compared with the cases at lower Reynolds numbers, the transition front at this Reynolds number is much closer to the fin leading edge, and two additional heat flux streaks (streak 3 and streak 4) appear. The heat streak near the corner (streak 3) is induced by the leading-edge streamwise vortices, formed by the fluid being driven toward the fin root due to the combined effect of the high pressure at the leading edge and the low pressure on the fin surface [4]. The other heat flux streak (streak 4) is located at the transition front; this streak has a relatively high heat flux, followed immediately by a turbulent heating region with a slightly lower heat flux.

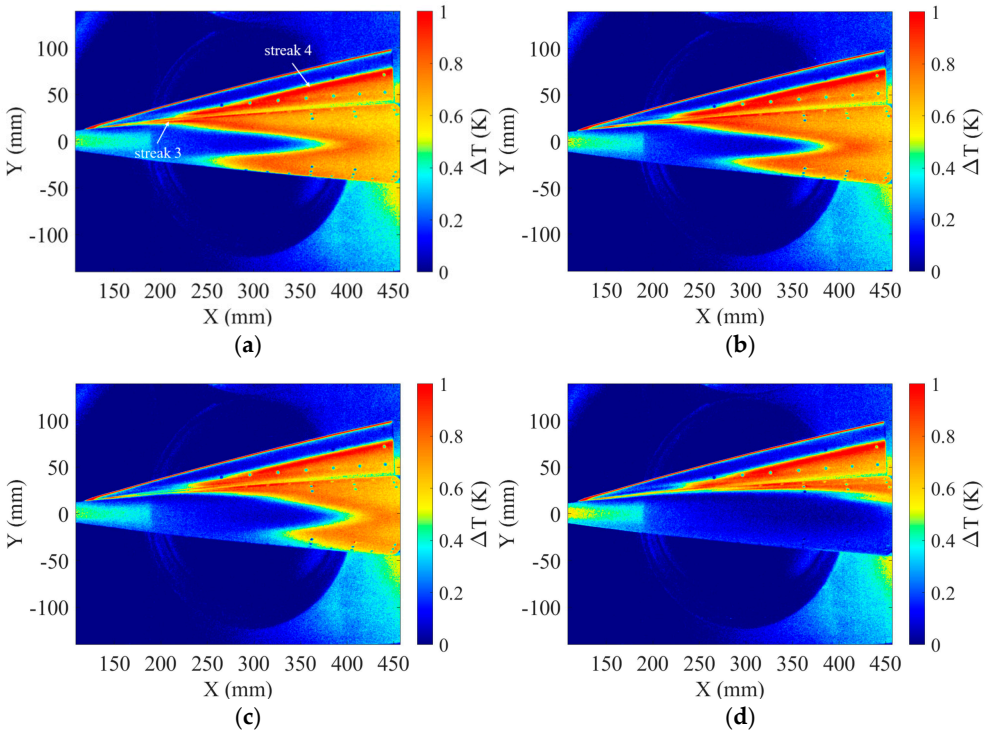


Figure 8. IR images of the leeward surface, $Re_\infty = 1.70 \times 10^7$ m^{-1}: (**a**) $R_n = 0.06$ mm; (**b**) $R_n = 0.56$ mm; (**c**) $R_n = 1.125$ mm; (**d**) $R_n = 2.34$ mm.

3.2. Windward Side

Figure 9 presents IR thermographic images of the windward surface of the fin–cone model under four different nose bluntness conditions at $Re_\infty = 6.09 \times 10^6$ m^{-1}. A prominent

heat streak (streak 5) is observed near the fin–cone corner, extending downstream from the junction with progressively decaying intensity. Another heat streak (streak 6), originating from the fin root leading edge and extending to the aft end of the model, is formed by the corner streamwise vortex induced by flow rollup in the corner region. A triangular high-heat-flux region is visible in the corner area, expanding from the corner toward the cone center (indicated by the red dashed line in Figure 9). This phenomenon is caused by the combined effect of corner streamwise vortex (streak 6) and boundary-layer transition. With increasing nose bluntness, the coverage of this high-heat-flux region on the cone surface is slightly reduced. In addition, a narrow low-heat-flux region is observed along the windward centerline. This feature results from the flow converging toward the centerline to form a streamwise vortex structure, leading to a thickened boundary layer and reduced heat flux. For all cases except R_n = 2.34 mm, the heat flux increases along and near the windward centerline further downstream, indicating the onset of transition. With increasing nose bluntness, the low-heat-flux region along the centerline expands both streamwise and spanwise, and the transition front shifts downstream. The transition front on both sides of the centerline exhibits a double-lobed pattern (indicated by the black dashed line in Figure 9), which is similar to the transition characteristics observed near the centerline of the HIFiRE-5 elliptic cone geometry by Juliano and Borg [21,22]. As the nose bluntness increases, the transition front along the centerline and its two sides shifts downstream, accompanied by a reduction in its spanwise extent. For the case with R_n = 0.06 mm, transition onset along the centerline occurs at X ≈ 150 mm, and the double-lobed pattern covers nearly the entire cone surface. When the nose radius increases to R_n = 0.56 mm, transition onset is delayed to X ≈ 200 mm, with the double-lobed front shifting downstream and contracting. With a further increase to R_n = 1.125 mm, the transition onset location is postponed to X ≈ 280 mm, and the lobed pattern becomes increasingly diffuse. In the case of R_n = 2.34 mm, the streamwise vortex reaches the largest scale, and the centerline as well as the adjacent regions remain laminar, with no transition observed. In contrast, the position of the fin surface transition front remains consistent under different bluntness conditions, which is consistent with the behavior on the leeward side.

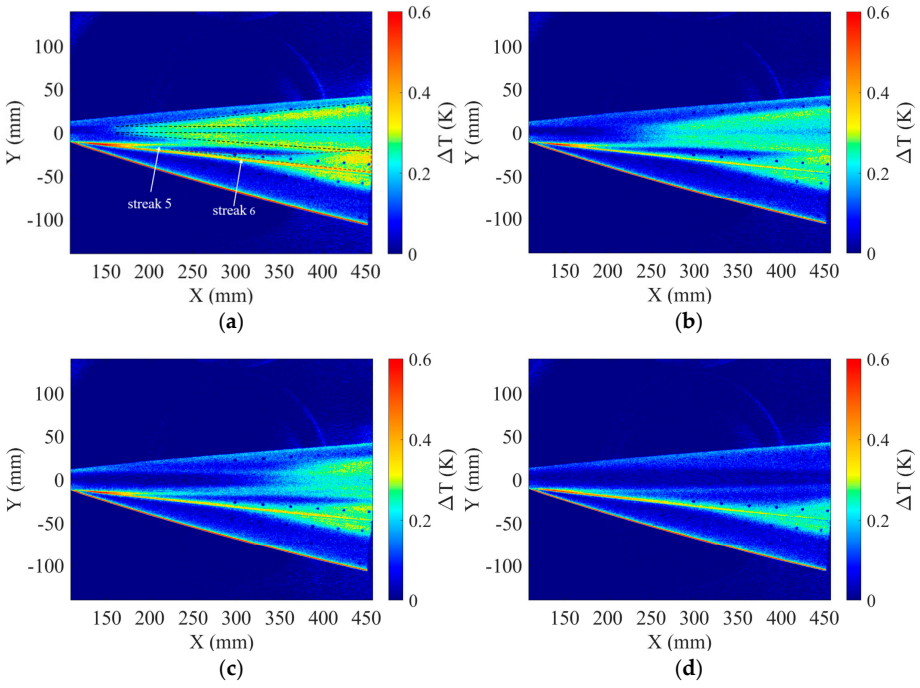


Figure 9. IR images of the windward surface, $Re_\infty = 6.09 \times 10^6$ m^{-1}: (**a**) R_n = 0.06 mm; (**b**) R_n = 0.56 mm; (**c**) R_n = 1.125 mm; (**d**) R_n = 2.34 mm.

When the freestream Reynolds number increases to $Re_\infty = 1.34 \times 10^7$ m^{-1}, as shown in Figure 10, the heat streaks formed by the horseshoe vortex become more prominent and shift toward the centerline. Compared with the low-Reynolds-number condition, the transition front on the cone surface shifts upstream with an expanded affected area. The transition front in the corner region merges with that extending bilaterally from the centerline, resulting in a gradual blurring of their boundary. Transition covers almost the entire cone surface at R_n = 0.06 mm, but gradually recedes with increasing nose bluntness. As the nose bluntness increases, the transition region on the cone surface gradually decreases. At R_n = 2.34 mm, transition is confined only to the corner region and the centerline near the model aft end. Additionally, higher Reynolds numbers shift the fin transition front further toward the leading edge.

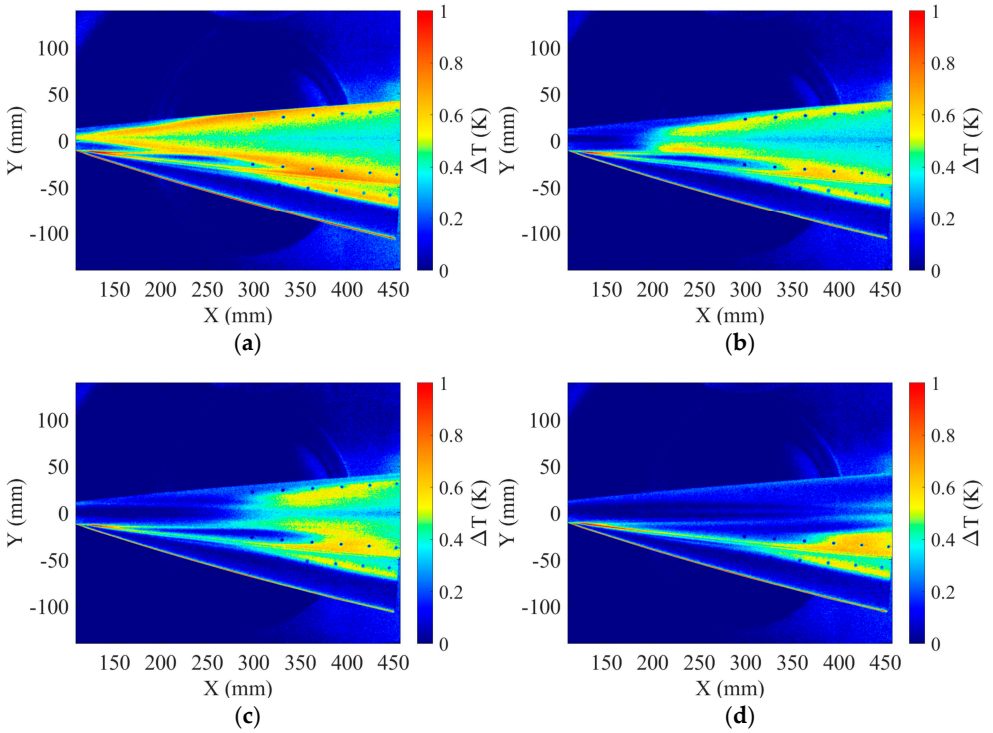


Figure 10. IR images of the windward surface, $Re_\infty = 1.34 \times 10^7$ m^{-1}: (**a**) R_n = 0.06 mm; (**b**) R_n = 0.56 mm; (**c**) R_n = 1.125 mm; (**d**) R_n = 2.34 mm.

A comparison of the IR images from the leeward and windward sides reveals that transition on the windward cone occurs earlier overall with a larger transition region, particularly evident at $Re_\infty = 6.09 \times 10^6$ m^{-1}. Under most bluntness conditions, extensive transition regions are observed along and near the windward centerline, while the flow remains largely laminar around the leeward centerline. This difference is caused by expansion waves generated by the double-cone structure on the leeward side, which suppress the growth of the second-mode instability and consequently delay transition. In contrast, the transition behavior on the fin surfaces shows the opposite trend: the transition front on the leeward fin is located closer to the leading edge than that on the windward side.

4. Analysis of Instability Waves

4.1. Leeward Side

4.1.1. WSC-L Region

Figure 11 presents the PSD results of pressure fluctuations along the A sensor ray near the leeward corner under different nose bluntness conditions at $Re_\infty = 6.09 \times 10^6$ m^{-1}. IR thermography indicates that under all bluntness conditions, PCB A1–A8 are almost located

on the primary heat streaks generated by the primary horseshoe vortex. For R_n = 0.06 mm, high-frequency instability waves (180–300 kHz) can be identified at PCB A1 and PCB A2. Along the downstream direction, the amplitude of the instability waves gradually increases, while their frequency does not show an obvious decreasing trend. By PCB A4, the characteristics of the instability waves disappear, and the flow is close to a fully developed turbulent state. When the bluntness increases to R_n = 0.56 mm, the amplitude of high-frequency instability waves at PCBs A1–A3 are reduced compared to the case of R_n = 0.06 mm. At R_n = 1.125 mm, only a weak high-frequency peak is observed at PCB A3. With a further increase in nose bluntness to R_n = 2.34 mm, instability waves are nearly undetectable. Although increasing nose bluntness reduces the amplitude of pressure fluctuations, transition under all four bluntness conditions occurs primarily between PCB A4 and PCB A5. This indicates that within this region, increasing the bluntness has a relatively limited effect on delaying boundary layer transition.

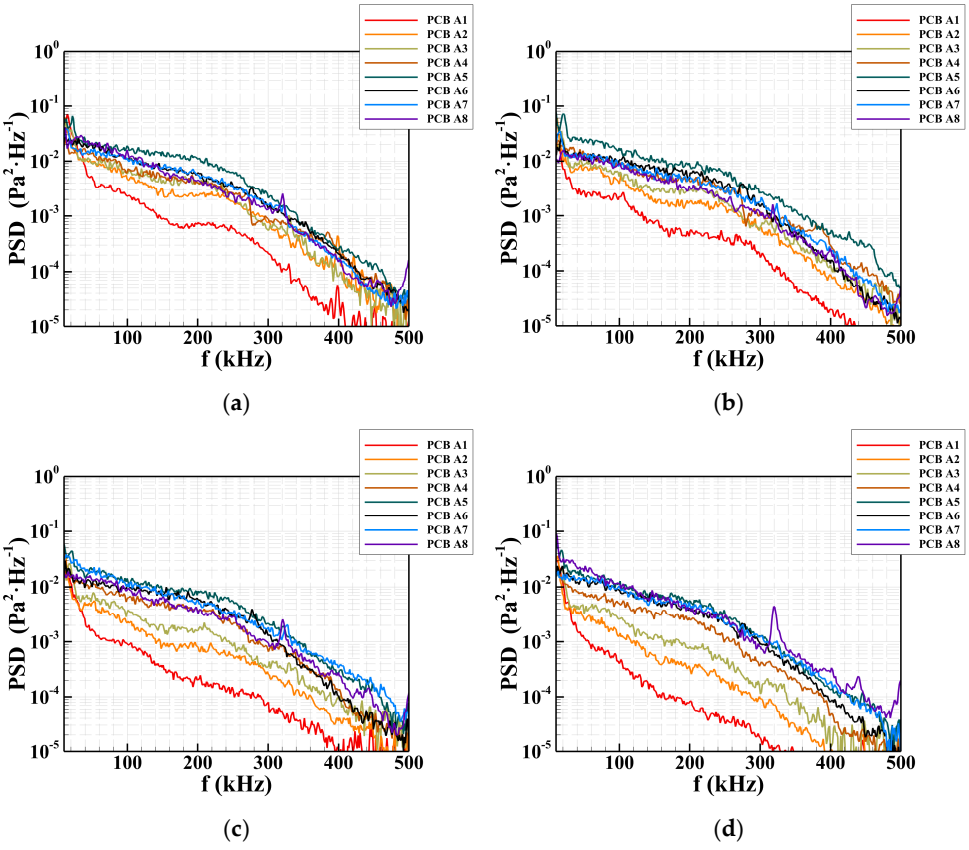


Figure 11. PSD results for the A sensor ray, $Re_\infty = 6.09 \times 10^6$ m^{-1}: (**a**) R_n = 0.06 mm; (**b**) R_n = 0.56 mm; (**c**) R_n = 1.125 mm; (**d**) R_n = 2.34 mm.

Figure 12 presents the PSD results of pressure fluctuations measured at PCB B1, B2, C1 and C2 under different nose bluntness conditions. At PCB B1, the flow is close to fully developed turbulence when R_n = 0.06 mm and R_n = 0.56 mm. As nose bluntness increases to R_n = 1.125 mm, a spectral swell emerges within the 100–250 kHz frequency range. Further increasing bluntness to R_n = 2.34 mm results in a narrowed frequency bandwidth, exhibiting a distinct spectral peak centered at approximately 150 kHz with reduced amplitude. At PCB B2, although the characteristics of instability waves are less pronounced, a consistent reduction in pressure fluctuation amplitude with increasing nose bluntness is observed. At PCB C1, located farther from the corner, all cases exhibit a spectral peak centered at 110 kHz. The frequency bandwidth of instabilities progressively narrows as nose bluntness increases. It is worth noting that for the R_n = 2.34 mm, PCB C1 is completely located outside the

streaks, which indicates that this peak is not related to the influence of the horseshoe vortex, thereby excluding the dominance of horseshoe vortex instability. Further downstream at PCB C2, the peak amplitude is higher, and the frequency bandwidth broadens, while the center frequency did not decrease significantly. This feature further ruled out the possibility of second-mode instability. Based on the aforementioned spectral characteristics and spatial positional relationships, it can be inferred that the instabilities observed at PCB C1 and PCB C2 correspond to traveling crossflow waves. At smaller bluntness levels, the boundary layer at PCB C2 has developed into turbulence. The above phenomena demonstrate that increasing nose bluntness exerts a relatively significant suppression effect on the instability waves in this region.

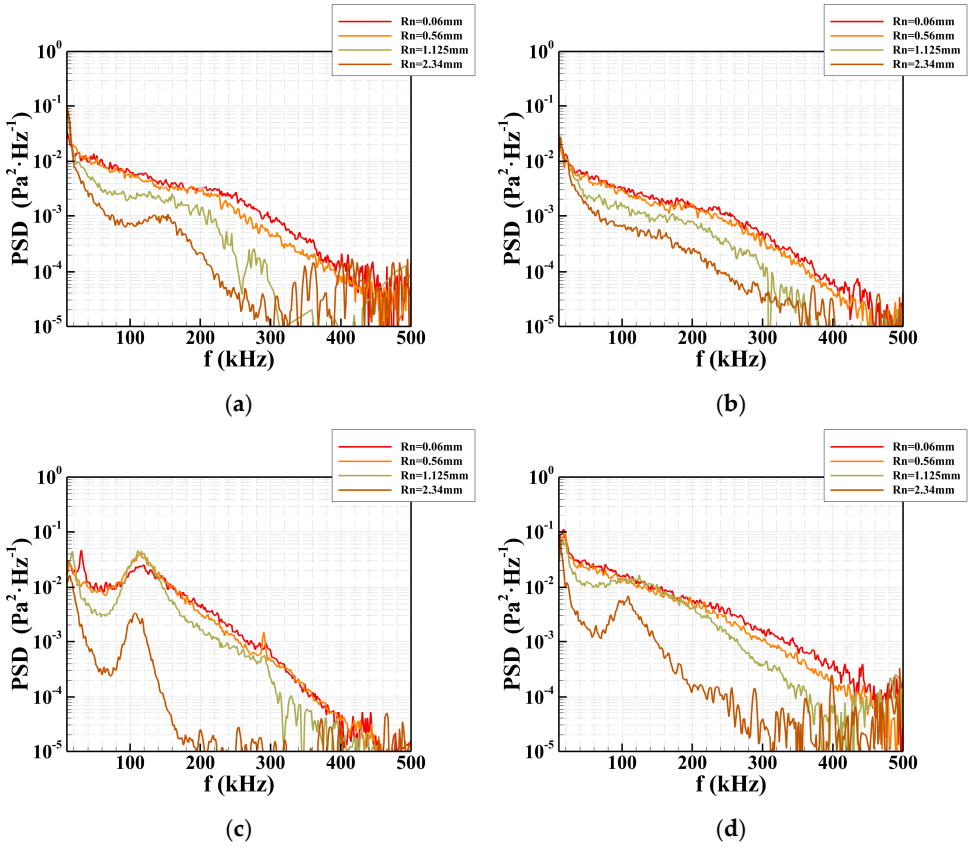


Figure 12. Comparison of PSD results at PCB B1, B2, C1 and C2 under four bluntness conditions, $Re_\infty = 6.09 \times 10^6$ m^{-1}: (**a**) PCB B1; (**b**) PCB B2; (**c**) PCB C1; (**d**) PCB C2.

To acquire more temporal and frequency-domain information about the signals from the inner streak, the CWT analysis method was performed on the signals from multiple PCB sensors arranged along the A sensor ray, which is closest to the corner. Figure 13 presents the CWT results at PCB A1–A5 with different nose radii under a freestream unit Reynolds number of $Re_\infty = 6.09 \times 10^6$ m^{-1}. For $R_n = 0.06$ mm, a narrowband peak with a center frequency of approximately 100 kHz, a mid-frequency peak at 100–200 kHz and a high-frequency peak at 200–300 kHz is observed at PCB A1. At PCB A2, the peak in the 200–300 kHz frequency band is significantly enhanced. Further downstream, disturbances gradually increase. By PCB A5, the frequency range covers nearly the entire spectrum, indicating that the boundary layer has fully transitioned to turbulence. When $R_n = 0.56$ mm, the peak frequency characteristics are similar to those in the $R_n = 0.06$ mm, but the distribution in the time series is less extensive. When the nose radius increases to $R_n = 1.125$ mm, the development of instability waves is delayed: only weak disturbances centered at 100 kHz are identified at PCB A1. The downstream disturbance evolution sequence is similar to that

of the small-nose case but occurs more downstream. For the largest nose bluntness case R_n = 2.34 mm, no obvious disturbances appear at PCB A1, and peaks centered at 100 kHz and within the 100–200 kHz frequency band are observed at PCB A2. However, at PCB A5, the flow still develops into a nearly fully turbulent state. The CWT results indicate that along the inner primary streak, although increasing the nose bluntness delays the initial formation and development of disturbance wavepackets, it has a relatively limited effect on the final transition location.

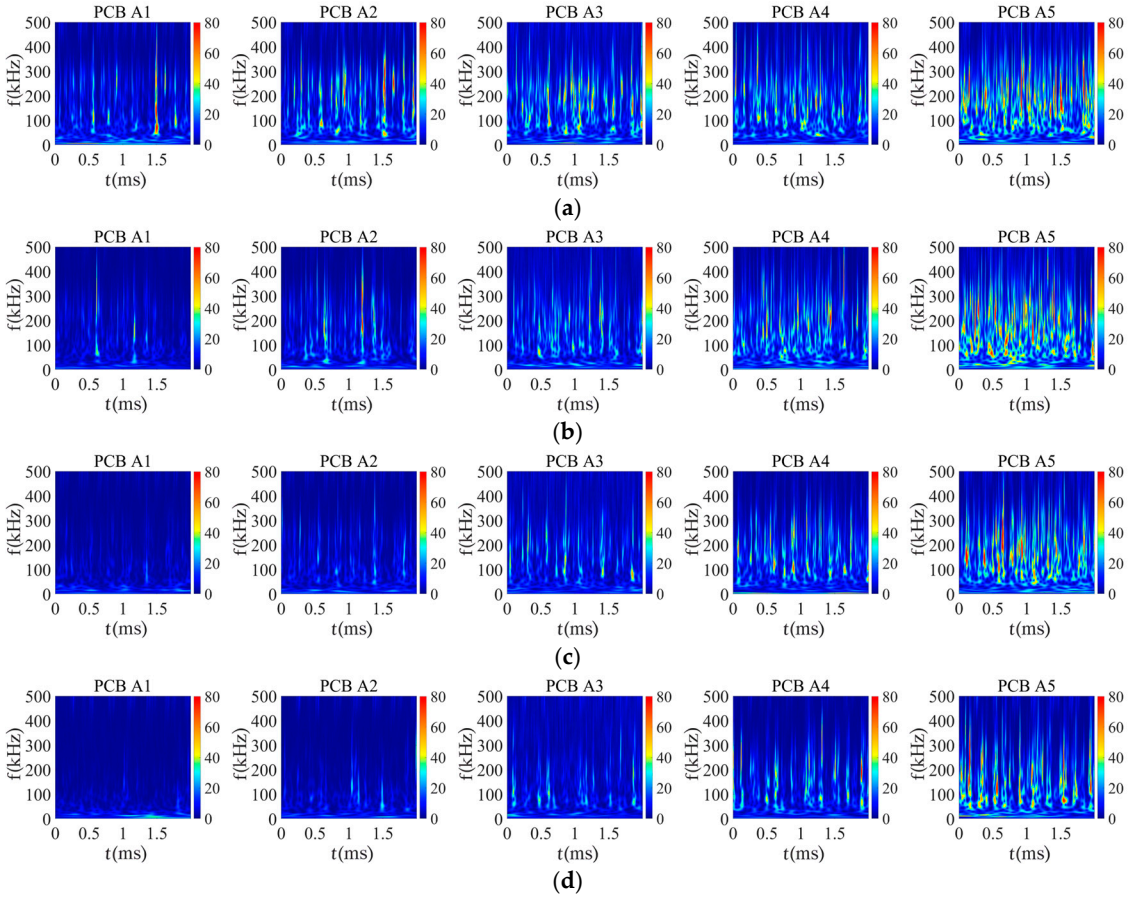


Figure 13. CWT results at PCB A1–A5, $Re_\infty = 6.09 \times 10^6$ m^{-1}: (**a**) R_n = 0.06 mm; (**b**) R_n = 0.56 mm; (**c**) R_n = 1.125 mm; (**d**) R_n = 2.34 mm.

These findings demonstrate that the flow adjacent to the primary streak in the WSC-L region is significantly influenced by the horseshoe vortex, resulting in highly complex flow dynamics. Previous studies have consistently identified diverse instabilities in this key region. Specifically, Knutson identified a strong crossflow instability near the fin–cone corner by using DNS [4]. Araya further verified the horseshoe vortex instability (centered around 250 kHz) near the fin–cone corner through multiple linear stability analysis methods [11]. Although the PSD results in Figure 11 failed to capture distinct instability signatures, the CWT results clearly reveal the presence of multiple isolated disturbance wavepackets. This phenomenon may be attributed to the coexistence of crossflow instability and horseshoe vortex instability within the boundary layer in this region. The non-synchronous coupling of these modes in the time domain leads to spectral broadening in the power spectrum. As the flow moves away from the fin–cone corner, the influence of the horseshoe vortex gradually weakens, and the frequency bandwidth narrows accordingly. When moving further away from the fin–cone corner, located near and predominantly outside the secondary streaks, crossflow instability appears to become the dominant mechanism.

Figure 14 presents the variation in the normalized Root Mean Square (RMS) value of pressure fluctuations with nose bluntness at representative sensor locations along rays A, B, and C (A1, B1, C2). Error bars in the figure indicate ±1 standard error. The RMS pressure fluctuations were obtained by integrating the PSD over the frequency range of 30–500 kHz and were subsequently normalized by the freestream static pressure. The results show that as the measurement locations move farther away from the fin–cone corner (from A1 to C2), the suppression of disturbance energy by increasing nose bluntness becomes significantly stronger. When the nose bluntness increases from R_n = 0.06 mm to R_n = 2.34 mm, the normalized RMS of pressure fluctuations decreases by approximately 55.4% at PCB A1 and reaches a reduction of 63.8% at PCB C2. This quantitative result demonstrates that, within the WSC-L region, the stabilizing effect of increased nose bluntness on boundary-layer instability intensifies with increasing distance from the fin root. This spatial dependence is likely attributable to the interaction between the fin shock and the cone shock in the fin–cone corner region, which generates a localized high-pressure, high-shear region. This shock structure may physically disrupt the direct influence of the upstream entropy layer on local receptivity processes, thereby potentially weakening the stabilizing effect of the increased nose bluntness in the corner region. In contrast, away from the shock interaction, the entropy layer directly influences boundary layer development, allowing the thickening from increased bluntness to fully exert its stabilizing effect and suppress instability waves.

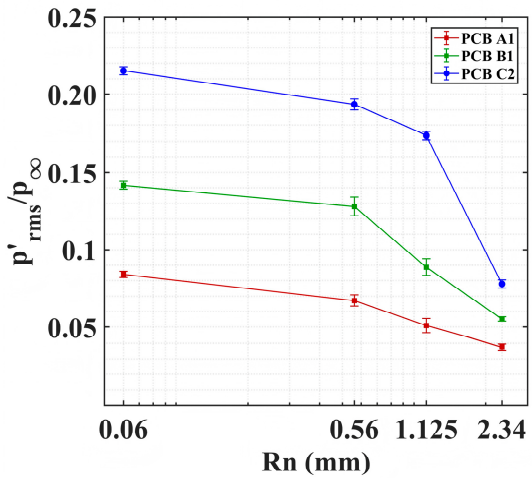


Figure 14. Variation in the normalized RMS of pressure fluctuations with nose bluntness at key sensor locations (PCB A1, B1, C2) on rays A, B, and C.

4.1.2. NSC-L Region

Figures 15–17 show, respectively, the PSD results measured along D, E, and F sensor rays on the fin-off side of the cone. The phenomena observed along the three rays are relatively similar. When R_n = 0.06 mm, R_n = 0.56 mm, and R_n = 1.125 mm, the instability waves and their development process along the downstream direction can be observed very clearly. As the flow develops downstream, the amplitude of the instability waves generally shows an increasing trend; meanwhile, as the boundary layer thickens, its peak frequency decreases significantly, which is consistent with the characteristics of typical second-mode instability. Cross-correlation analysis was performed on the signals from adjacent sensors PCB D1 and D2 to obtain the propagation velocity of the instability waves, R_n = 0.56 mm taken as the representative case. The distance between the two sensors is ΔL = 22.5 mm. As shown in Figure 18, the cross-correlation peak yields a time lag Δt = 0.02916 ms. The velocity at the outer edge of the boundary layer is to be about U_e = 831.68 m/s. The computed propagation speed is u = 771.6 m/s, approximately 92.8% of U_e. This value lies within the theoretical slow-mode phase-velocity range of the second

mode, $[1 - \frac{1}{Ma}, 1]$, providing further confirmation that the observed instability waves are second-mode waves. The central frequency of these instability waves ranges from 100 to 200 kHz. As the nose radius increases, the amplitude of the instability waves at the same PCB location decreases significantly, and their onset is also delayed. When the nose radius increases to R_n = 2.34 mm, the instability waves have barely developed; only a weak peak appears at PCB F2 and F3.

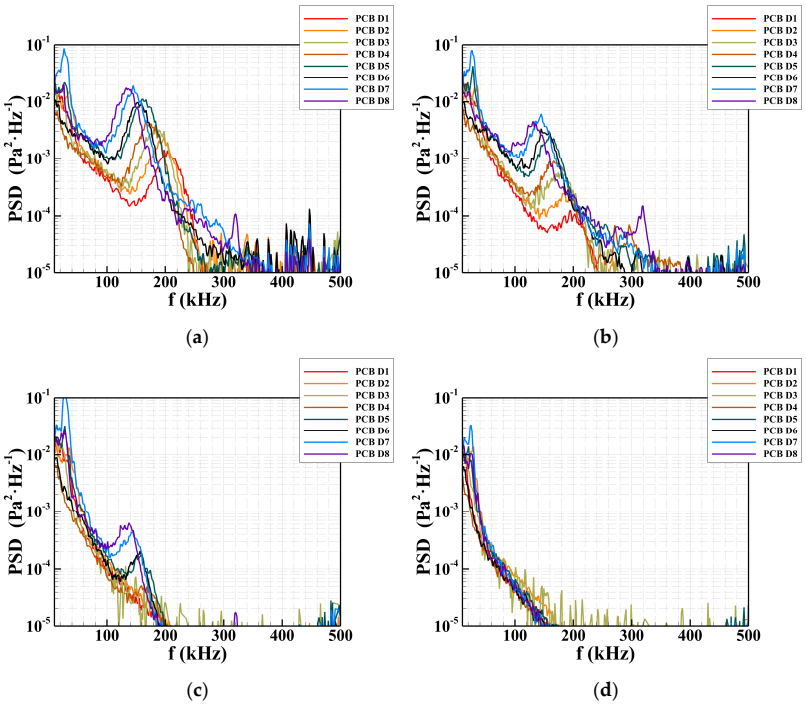


Figure 15. PSD results for the D sensor ray, $Re_\infty = 6.09 \times 10^6$ m^{-1}: (**a**) R_n = 0.06 mm; (**b**) R_n = 0.56 mm; (**c**) R_n = 1.125 mm; (**d**) R_n = 2.34 mm.

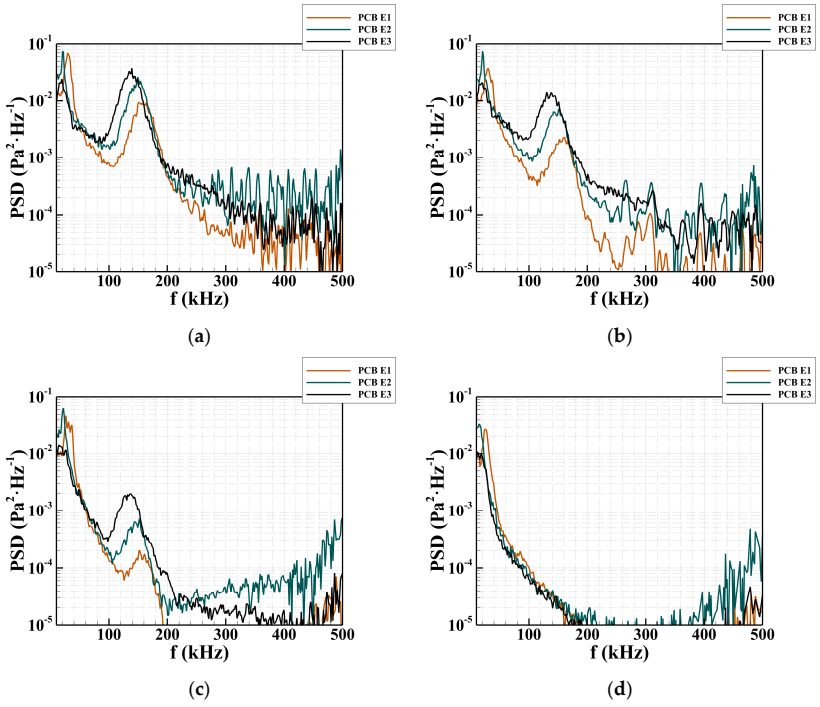


Figure 16. PSD results for the E sensor ray, $Re_\infty = 6.09 \times 10^6$ m^{-1}: (**a**) R_n = 0.06 mm; (**b**) R_n = 0.56 mm; (**c**) R_n = 1.125 mm; (**d**) R_n = 2.34 mm.

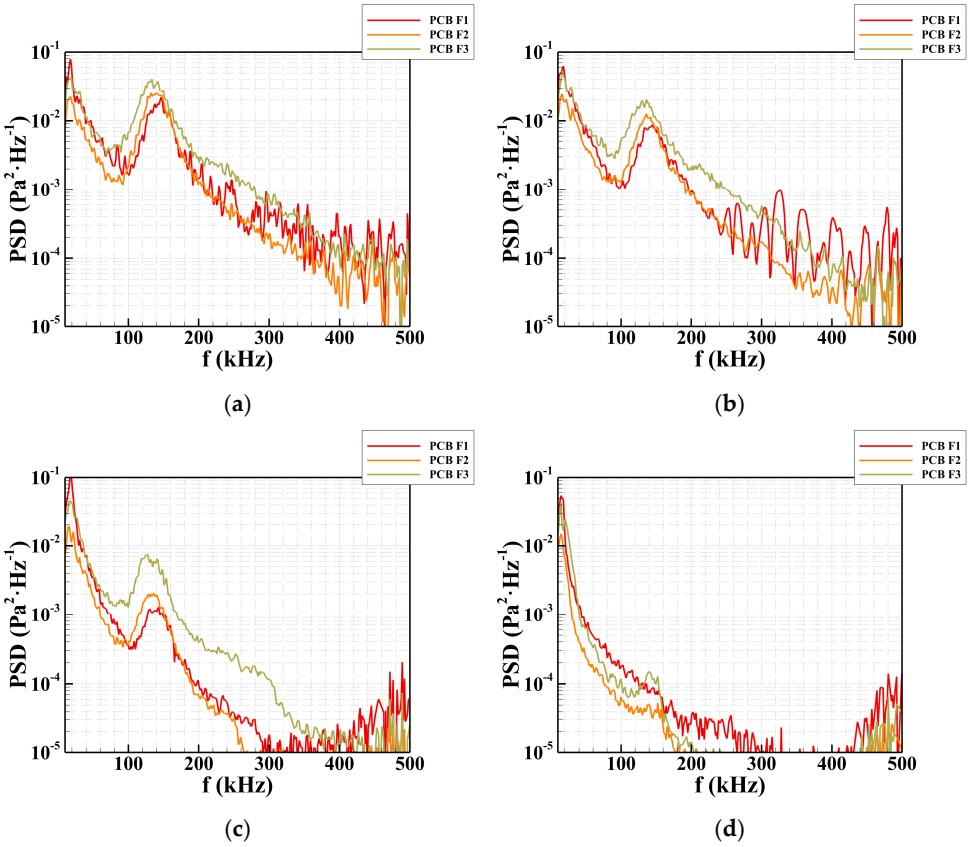


Figure 17. PSD results for the F sensor ray, $Re_\infty = 6.09 \times 10^6$ m^{-1}: (**a**) $R_n = 0.06$ mm; (**b**) $R_n = 0.56$ mm; (**c**) $R_n = 1.125$ mm; (**d**) $R_n = 2.34$ mm.

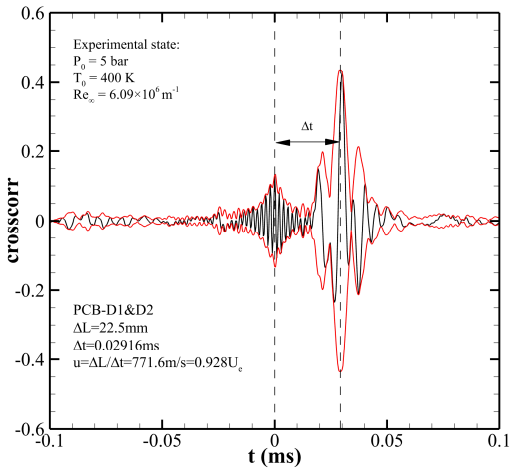


Figure 18. Cross-correlation curves between PCB D1 and D2: the black curve denotes the cross-correlation function of signals from the two sensors, and the red curve represents its envelope curve.

These phenomena indicate that within the NSC-L region, boundary-layer transition is primarily dominated by second-mode instability. This instability mode is relatively sensitive to changes in nose bluntness: as nose bluntness increases, the development of second-mode instability is significantly suppressed, with reduced amplitude and delayed onset. Eventually, under relatively high nose bluntness, the boundary layer tends to be fully laminarized, and instability waves almost disappear. This phenomenon is highly consistent with the findings of Huang regarding the effect of bluntness on boundary-layer transition in sharp cone model [23].

4.1.3. Fin Region

Figure 19 presents the PSD results measured along the G sensor ray on the leeward side of the fin. The power spectra under four nose bluntness conditions exhibit a similar pattern: at PCB G1–G3, high-frequency instability waves with a central frequency of approximately 180 kHz can be observed in all cases. Their amplitude gradually increases along the streamwise direction; by PCB G4, spectral broadening occurs in the power spectrum, and finally, the flow fully develops into turbulence at PCB G5. Knutson has confirmed the existence of significant crossflow on the fin surface, and pointed out that the ratio of the maximum crossflow velocity to the boundary layer edge velocity (u_{cf}/U_e) is as high as 33% [4]. Furthermore, by arranging square array pressure sensors on the fin surface and combining phase analysis with linear coherence verification, Middlebrooks et al. clearly identified traveling crossflow waves with a frequency of approximately 117.9 kHz [24]. Based on these findings, it is reasonable to suggest that boundary-layer transition on the fin may be dominated by crossflow instability, and from the perspective of spectral characteristics, the high-frequency instability waves observed at PCB G1–G3 most likely correspond to traveling crossflow modes. Notably, as nose bluntness increases, the amplitude of instability waves and the transition location remain largely unchanged. This indicates that variations in nose bluntness have a negligible effect on the transition process on the fin surface. This phenomenon may be attributed to the fact that the crossflow on the fin is primarily governed by its sweep angle and the local pressure gradient, while the effect of nose bluntness on the upstream flow—transmitted through the entropy layer and the bow shock structure—undergoes substantial attenuation before reaching the fin surface, resulting in a local crossflow velocity profile that is largely insensitive to nose conditions. Appendix B presents the numerical simulation results of boundary layer and entropy layer evolution.

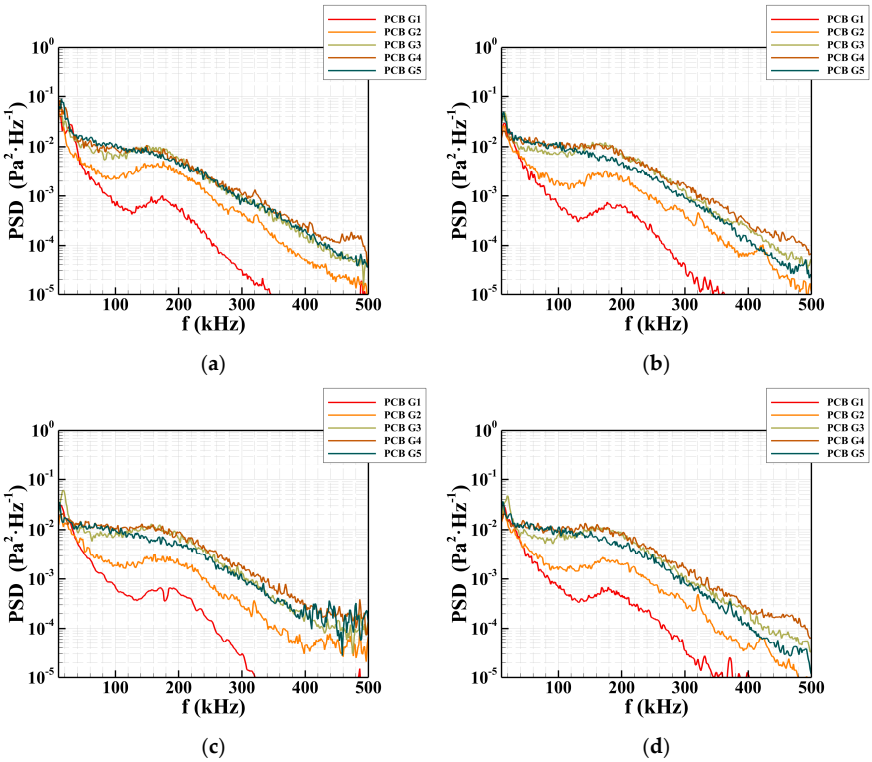


Figure 19. PSD results for the G sensor ray, $Re_\infty = 6.09 \times 10^6$ m^{-1}: (**a**) $R_n = 0.06$ mm; (**b**) $R_n = 0.56$ mm; (**c**) $R_n = 1.125$ mm; (**d**) $R_n = 2.34$ mm.

4.2. Windward Side

4.2.1. WSC-W Region

Figure 20 presents the PSD results measured along the H sensor ray near the corner on the windward side under different nose bluntness conditions at $Re_\infty = 6.09 \times 10^6$ m^{-1}. The result shows that a high-frequency instability wave exists in this region across all four nose bluntness conditions, with its frequency range approximately between 160 and 300 kHz. For the $R_n = 0.06$ mm, a small swell appears at PCB H1. Further downstream at PCB H2, this disturbance develops into a distinct broadband instability wave, which nearly disappears at PCB H3 and transitions to turbulence by PCB H4. Although increasing nose bluntness suppresses the amplitude of instability waves at upstream locations such as PCB H1, with no disturbances even detected at PCB H1 for the case of $R_n = 2.34$ mm, the flow characteristics become increasingly similar farther downstream. At PCB H3, the spectra already exhibit broadening with comparable amplitude levels, and the flow is about to transition to turbulence across all bluntness conditions. This result indicates that, within this region, variations in nose bluntness exert a limited influence on the final transition location. IR image results confirm that while the measurement points are not on the horseshoe vortex path, they lie within the zone of mutual interference between the fin shock and the cone shock. The observed insensitivity of boundary-layer transition in this region to nose bluntness variations further demonstrates that the local flow structure generated by this shock interaction effectively blocks the direct influence of the nose on local receptivity processes. Furthermore, the disturbance exhibits no frequency decay in the streamwise direction, and its spectral characteristics differ significantly from the second-mode frequencies measured later in the NSC-W region. Based on these combined features, the observed high-frequency instability waves are inferred to be traveling crossflow modes.

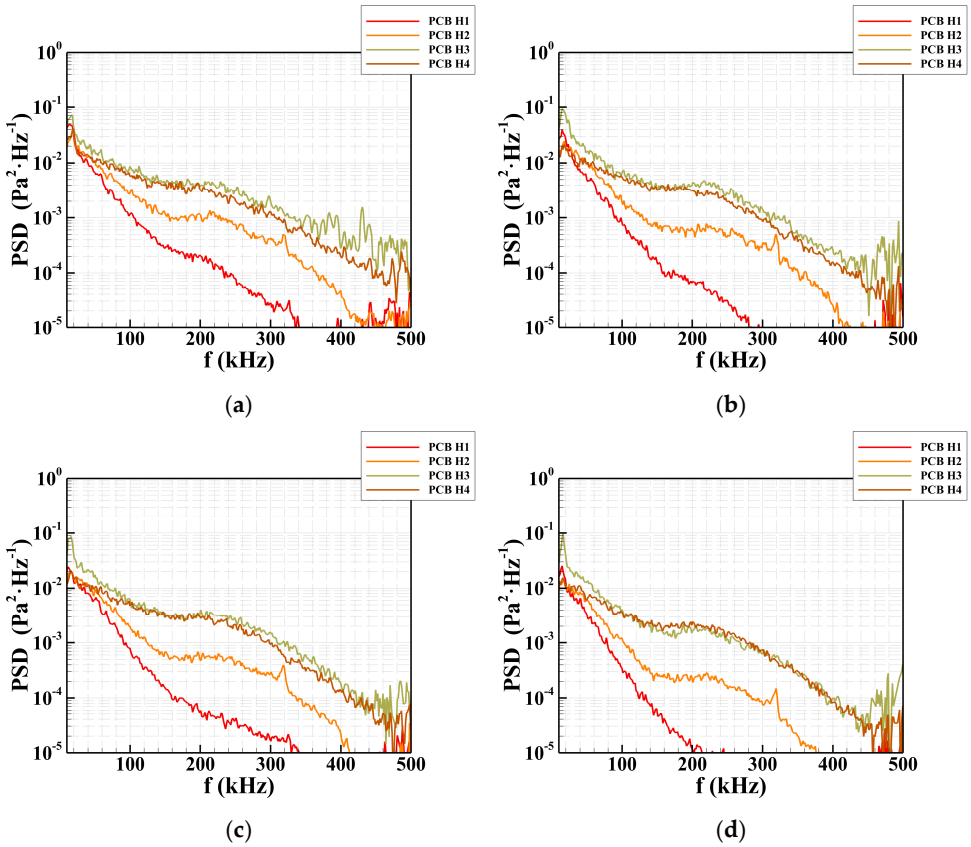


Figure 20. PSD results for the H sensor ray, $Re_\infty = 6.09 \times 10^6$ m^{-1}: (**a**) $R_n = 0.06$ mm; (**b**) $R_n = 0.56$ mm; (**c**) $R_n = 1.125$ mm; (**d**) $R_n = 2.34$ mm.

4.2.2. NSC-W Region

Figure 21 presents the PSD results measured along the J sensor ray on the fin-off side of the cone. For the R_n = 0.06 mm and R_n = 0.56 mm configurations, high-frequency instability waves are detected at PCB J1–J6, with their central frequency gradually decreasing from 180 kHz to 150 kHz along the downstream direction. As nose bluntness increases, the amplitude of instability waves at the same PCB locations is strongly suppressed, and their onset is significantly delayed. For the R_n = 1.125 mm case, instability waves do not emerge until PCB J4. Under the R_n = 2.34 mm condition, all measurement locations are in a fully laminar state. Similarly to the case in the NSC-L region, the evolution characteristics of these high-frequency instability waves are consistent with those of second-mode waves. Cross-correlation analysis between PCB J1 and J2 for the R_n = 0.56 mm case is shown in Figure 22. The computed propagation speed is u = 810.94 m/s, approximately 97.5% of U_e, further confirming this interpretation. Likewise, increasing nose bluntness can effectively suppress boundary-layer transition in this region.

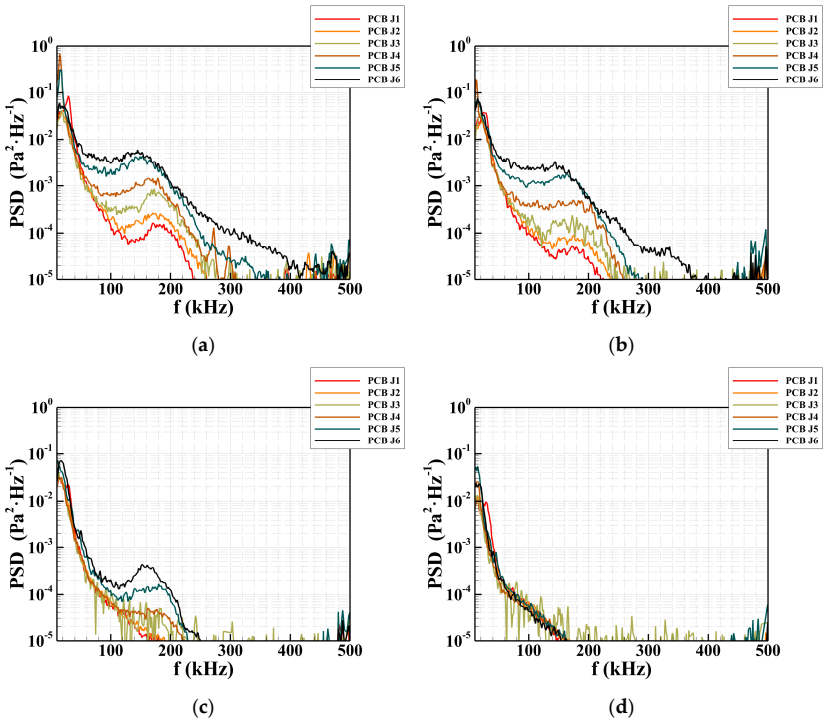


Figure 21. PSD results for the J sensor ray, $Re_\infty = 6.09 \times 10^6$ m^{-1}: (**a**) R_n = 0.06 mm; (**b**) R_n = 0.56 mm; (**c**) R_n = 1.125 mm; (**d**) R_n = 2.34 mm.

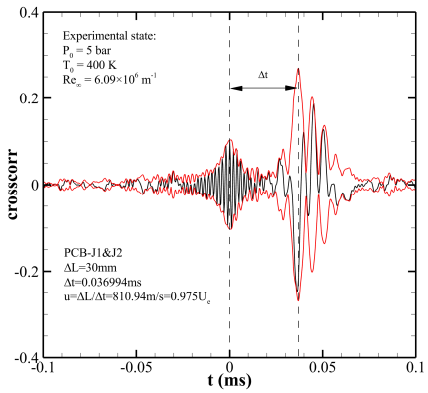


Figure 22. Cross-correlation curves between PCB J1 and J2: the black curve denotes the cross-correlation function of signals from the two sensors, and the red curve represents its envelope curve.

4.2.3. Fin Region

Figure 23 presents the PSD results measured along the K sensor ray on the windward side of the fin. The spectral characteristics show a high degree of consistency across all four bluntness ratios. Instability waves become prominent starting at PCB K2, grow gradually downstream, and begin to diminish at PCB K5, where spectral broadening occurs, and the flow fully turns into turbulence at PCB K6. The central frequency of the instability waves at all measurement locations remains stable at approximately 140 kHz and does not change with the streamwise position. Based on its spectral characteristics, the instability wave can be inferred as a traveling crossflow wave. Similarly to the situation on the leeward side, variations in nose bluntness show no significant effect on the boundary-layer transition process over the fin surface. It is noteworthy that, at the same streamwise location, the central frequency of the instability wave on the windward side is lower than the corresponding value observed on the leeward side. This difference may result from the inherent distinctions in local pressure gradients and crossflow velocity profiles between the windward and leeward sides.

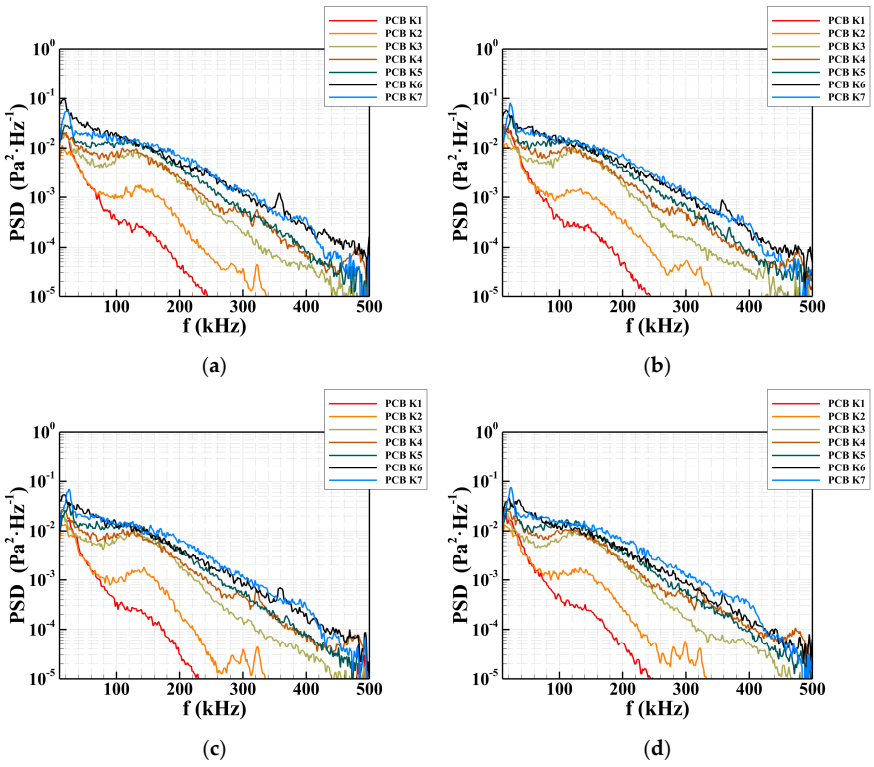


Figure 23. PSD results for the K sensor ray, $Re_\infty = 6.09 \times 10^6$ m^{-1}: (**a**) $R_n = 0.06$ mm; (**b**) $R_n = 0.56$ mm; (**c**) $R_n = 1.125$ mm; (**d**) $R_n = 2.34$ mm.

5. Conclusions

Experimental investigations on the hypersonic boundary-layer transition of a fin–cone configuration were conducted in a Mach 6 Ludwieg tube tunnel at HUST. Infrared thermography was used to obtain the distribution of transition fronts, and PCB high-frequency pressure sensors were employed to characterize the instability waves in different regions of the model, with a focus on the effect of nose bluntness on boundary-layer instability. The transition characteristics differ across regions. On the leeward cone surface, transition is delayed near the centerline due to expansion waves generated by the double-cone structure. Meanwhile, the region close to the corner is significantly influenced by the horseshoe vortex, forming two heat flux streaks. As the flow moves away from the streaks, instability waves around 110 kHz emerge, likely associated with traveling crossflow

modes. In contrast, on the windward cone surface, transition occurs earlier and broadband high-frequency instability waves around 160–300 kHz are observed near the corner, which are inferred as traveling crossflow waves. On the fin-off side of the cone, both on the leeward and windward surfaces, transition is dominated by the second mode, while on the fin surface, it is likely dominated by crossflow instability. The suppressive effect of increased nose bluntness on cone transition strengthens with distance from the fin root, especially near the centerline and on the fin-off side, yet remains limited in shock-interaction regions near the fin–cone corner. Nevertheless, increasing nose bluntness can suppress the horseshoe vortex development on the cone surface. Additionally, transition on the fin surface is insensitive to nose bluntness variations.

This study provides a preliminary understanding and a data foundation for the aerodynamic design and transition prediction of complex aircraft configurations. Future work should combine numerical and experimental approaches to precisely identify and quantify the dominant instability modes and their evolution.

Author Contributions: Conceptualization, Z.F.; methodology, Z.F.; software, Z.F.; validation, Z.F., L.X. and D.X.; formal analysis, Z.F.; investigation, Z.F. and J.W.; resources, J.W.; data curation, Z.F.; writing—original draft preparation, Z.F.; writing—review and editing, Z.F. and X.L.; visualization, Z.F.; supervision, J.W. and F.Z.; project administration, J.W. and F.Z.; funding acquisition, F.Z. All authors have read and agreed to the published version of the manuscript.

Funding: This research was funded by the National Natural Science Foundation of China (12472334).

Data Availability Statement: Dataset available on request from the authors.

Acknowledgments: The authors are grateful for the assistance during the experiments provided by Dailin Lv from Huazhong University of Science and Technology.

Conflicts of Interest: The authors declare no conflicts of interest.

Abbreviations

The following abbreviations are used in this manuscript:

DNS	Direct Numerical Simulation
BAM6QT	Boeing/AFOSR Mach-6 Quiet Tunnel
IR	Infrared
HUST	Huazhong University of Science and Technology
PSD	Power Spectral Density
CWT	Continuous Wavelet Transform
WSC	Wing Side Cone
NSC	Non-wing Side Cone
RMS	Root Mean Square

Appendix A

The specific locations of the sensors on the model are detailed in Tables A1–A5.

Table A1. Sensor positions along the A and D sensor rays.

Sensor Numbers	X (mm)	Y (mm)
PCB A1/D1	287.87	±27.98
PCB A2/D2	310.28	±29.58
PCB A3/D3	332.70	±31.14
PCB A4/D4	355.13	±32.67
PCB A5/D5	377.55	±34.16
PCB A6/D6	399.98	±35.61
PCB A7/D7	422.41	±37.03
PCB A8/D8	444.85	±38.39

Table A2. Sensor positions along the B and E sensor rays.

Sensor Numbers	X (mm)	Y (mm)
PCB B1/E1	354.50	±28.47
PCB B2/E2	399.35	±31.38
PCB B3/E3	444.21	±34.19

Table A3. Sensor positions along the C and F sensor rays.

Sensor Numbers	X (mm)	Y (mm)
PCB C1/F1	354.55	±23.09
PCB C2/F2	399.39	±25.99
PCB C3/F3	444.24	±28.87

Table A4. Sensor positions along the H and J sensor rays.

Sensor Numbers	X (mm)	Y (mm)
PCB H1/J1	294.75	±21.16
PCB H2/J2	324.67	±23.22
PCB H3/J3	354.58	±25.28
PCB H4/J4	384.50	±27.35
PCB H5/J5	414.41	±29.43
PCB H6/J6	444.33	±31.51

Table A5. Sensor positions along the G and K sensor rays.

Sensor Numbers	X (mm)	Y (mm)
PCB G1/K1	261.83	9.04
PCB G2/K2	291.69	9.23
PCB G3/K3	321.54	9.45
PCB G4/K4	351.40	9.73
PCB G5/K5	381.25	10.07
PCB G6/K6	411.11	10.47
PCB G7/K7	440.97	10.95

Appendix B

To evaluate the development of the boundary layer and entropy layer, steady-state flow-field numerical simulations were conducted for two bluntness configurations: R_n = 0.06 mm and R_n = 2.34 mm. The governing equations consist of the three-dimensional compressible Navier–Stokes equations, solved using a finite-volume approach. The freestream conditions were specified as follows: static pressure P = 443.35 Pa, static temperature T_∞ = 48.78 K, and freestream Reynolds number $Re_\infty = 8.52 \times 10^6$ m^{-1}. Due to the short effective runtime of the wind tunnel, an isothermal wall condition (T_w = 300 K) was applied on the model surface. Pressure-far-field conditions were applied at the boundaries of the computational domain.

Figure A1 presents the overall grid topology of the computational domain. A fully structured multi-block mesh was employed to discretize the three-dimensional computational domain. The mesh contains 571, 397, and 553 grid points in the streamwise, wall-normal, and spanwise directions, respectively, yielding approximately 120 million grid cells in total. Mesh refinement and smooth transitions were applied in regions with significant flow gradients, such as the nose, boundary layer, and fin–cone junction. The

wall-normal height of the first grid layer was set to 0.001 mm to ensure that y+ < 1 across the entire computational domain.

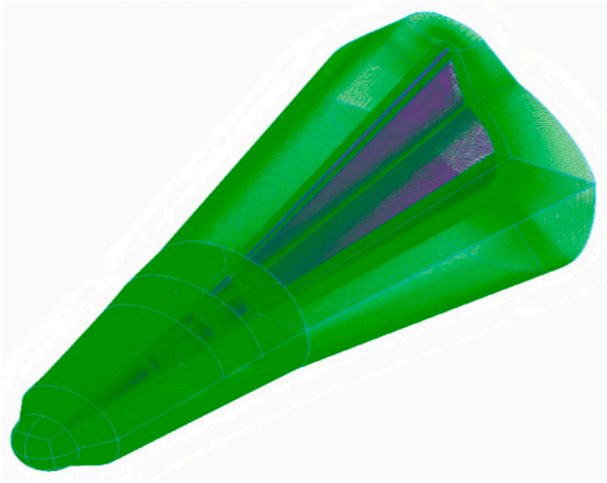


Figure A1. Overall grid topology.

Flow-field profiles were extracted along the symmetry plane of the fin, and the streamwise evolution of the boundary layer and entropy layer is shown in Figures A2 and A3. The boundary-layer thickness δ_h is defined as the location where the total enthalpy recovers to 99.5% of the freestream total enthalpy, satisfying $h_t(\delta_h) = 0.995 h_{t\infty}$, where the total enthalpy is $h_t = h + 0.5(u^2 + v^2 + w^2)$ and the static enthalpy is $h = C_p T$. This definition follows the method used by Paredes et al. [25]. The entropy-layer thickness δ_s is calculated using $\Delta S(\delta_s) = 0.25 \Delta S_{\text{wall}}$, $\Delta S = \frac{\gamma}{\gamma - 1} \ln\left(\frac{T}{T_\infty}\right) - \ln\left(\frac{P}{P_\infty}\right)$, where the specific-heat ratio is $\gamma = 1.4$. This definition of entropy-layer thickness is adopted from Hartman et al. [26]. As can be seen from the figures, the entropy-layer thickness increases significantly with the nose bluntness, while the boundary-layer thickness increases only slightly. For R_n = 0.06 mm, the difference in thickness between the entropy layer and the boundary layer is relatively small. The entropy layer merges into the boundary layer before reaching the fin surface (X ≈ 99.57 mm), exhibiting entropy-swallowing behavior. For R_n = 2.34 mm, the entropy layer near the nosetip is much thicker than the boundary layer. Its thickness first increases along the streamwise direction to a maximum and then gradually decreases. When approaching the fin surface, it progressively converges toward the local boundary-layer thickness. The above two cases indicate that the influence of bluntness on the upstream flow through the entropy layer undergoes significant attenuation before reaching the fin surface.

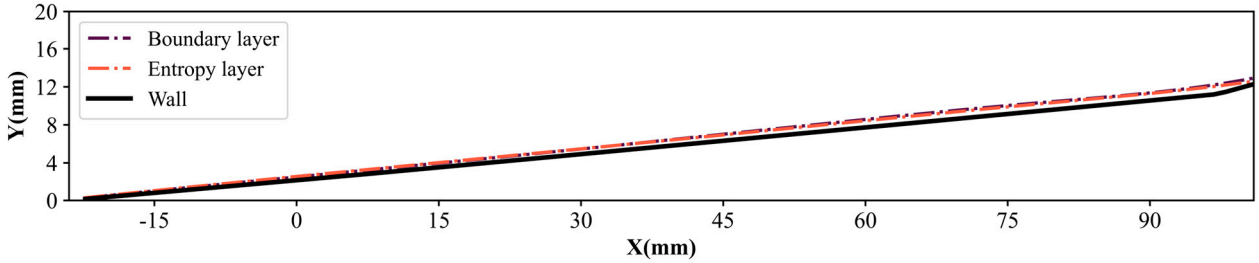


Figure A2. Development of the boundary-layer and entropy-layer thicknesses, R_n = 0.06 mm.

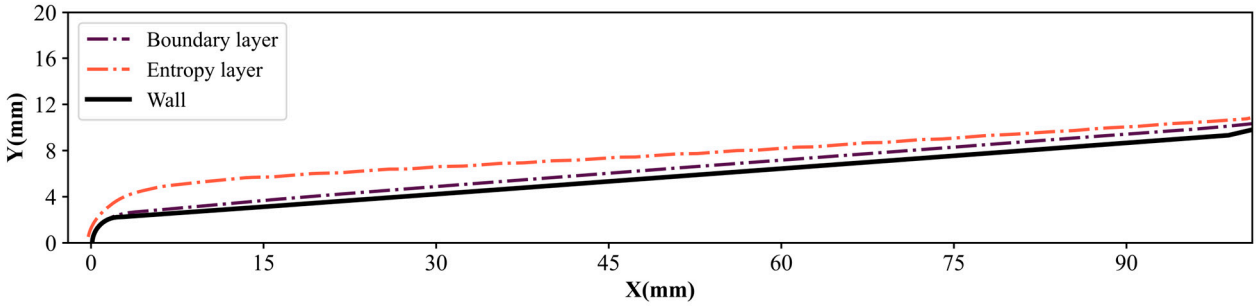


Figure A3. Development of the boundary-layer and entropy-layer thicknesses, R_n = 2.34 mm.

References

1. Chen, J.; Yuan, X.; Tu, G.; Chen, J.; Zhang, Y.; Xu, G.; Tong, F.; Wan, B. Recent Progress on Hypersonic Boundary-Layer Transition. *Sci. China Phys. Mech. Astron.* **2019**, *49*, 125–138.
2. Li, X.; Xu, B.; Huang, G.; Wu, J. Experimental Study on the Boundary-Layer Transition of a High-Speed Fin-Cone Configuration. *Adv. Aerodyn.* **2025**, *7*, 10. [CrossRef]
3. Middlebrooks, J.B.; Peck, M.M.; Farnan, E.L.; Matlis, E.; Juliano, T.J.; Corke, T.C.; Mullen, D.; Reed, H.; Semper, M.T. Crossflow Instability on a Swept Fin–Cone with Variable Nose Bluntness in Mach 6 Flow. *AIAA J.* **2024**, *62*, 2036–2050. [CrossRef]
4. Knutson, A.; Gs, S.; Candler, G.V. Direct Numerical Simulation of Mach 6 Flow over a Cone with a Highly Swept Fin. In Proceedings of the 2018 AIAA Aerospace Sciences Meeting, Kissimmee, FL, USA, 8–12 January 2018; American Institute of Aeronautics and Astronautics: Reston, VA, USA, 2018.
5. Knutson, A.; Gs, S.; Candler, G.V. Instabilities in Mach 6 Flow over a Cone with a Swept Fin. In Proceedings of the 2018 Fluid Dynamics Conference, Atlanta, GA, USA, 25–29 June 2018; American Institute of Aeronautics and Astronautics: Reston, VA, USA, 2018.
6. Mullen, C.D.; Moyes, A.; Kocian, T.S.; Reed, H.L. Parametric Boundary-Layer Stability Analysis on a Hypersonic Finned Circular Cone. In Proceedings of the 2018 Fluid Dynamics Conference, Atlanta, GA, USA, 25–29 June 2018; American Institute of Aeronautics and Astronautics: Reston, VA, USA, 2018.
7. Mullen, C.D.; Moyes, A.; Kocian, T.S.; Reed, H.L. Heat Transfer and Boundary-Layer Stability Analysis of Subscale BOLT and the Fin Cone. In Proceedings of the AIAA Aviation 2019 Forum, Dallas, TX, USA, 17–21 June 2019; American Institute of Aeronautics and Astronautics: Reston, VA, USA, 2019.
8. Turbeville, F.D.; Schneider, S.P. Boundary-Layer Instability on a Slender Cone with Highly Swept Fins. In Proceedings of the 2018 Fluid Dynamics Conference, Atlanta, GA, USA, 25–29 June 2018; American Institute of Aeronautics and Astronautics: Reston, VA, USA, 2018.
9. Turbeville, F.D.; Schneider, S.P. Transition on a Cone with a Highly-Swept Fin at Mach 6. In Proceedings of the AIAA Aviation 2019 Forum, Dallas, TX, USA, 17–21 June 2019; American Institute of Aeronautics and Astronautics: Reston, VA, USA, 2019.
10. Turbeville, F.D.; Schneider, S.P. Effect of Nose Bluntness on Fin-Cone Transition at Mach 6. In Proceedings of the AIAA Aviation 2021 Forum, Virtual Event, 2–6 August 2021; American Institute of Aeronautics and Astronautics: Reston, VA, USA, 2021.
11. Araya, D.; Bitter, N.; Wheaton, B.M.; Kamal, O.; Colonius, T.; Knutson, A.; Johnson, H.; Nichols, J.; Candler, G.V.; Russo, V.; et al. Assessment of Linear Methods for Analysis of Boundary Layer Instabilities on a Finned Cone at Mach 6. In Proceedings of the AIAA Aviation 2022 Forum, Chicago, IL, USA & Virtual, 27 June–1 June 2022; American Institute of Aeronautics and Astronautics: Reston, VA, USA, 2022.
12. Middlebrooks, J.B.; Farnan, E.; Juliano, T.J.; Matlis, E.H.; Corke, T.C.; Peck, M.M.; Mullen, D.; Reed, H.L.; Semper, M. Cross-Flow Instability Experiments on a Swept Fin-Cone with Variable Nose Bluntness in Mach 6 Flow. In Proceedings of the AIAA SciTech 2022 Forum, San Diego, CA, USA & Virtual, 3–7 January 2022; American Institute of Aeronautics and Astronautics: Reston, VA, USA, 2022.
13. Huang, R.; Zhang, C.; Li, C.; Xu, B.; Xu, D.; Yuan, X.; Wu, J. Design and Preliminary Freestream Calibration of HUST Φ 0.5 m Mach 6 Ludwieg Tube Wind Tunnel. *Acta Aerodyn. Sin.* **2023**, *41*, 39–48.
14. Li, X.; Li, C.; Su, W.; Wu, J. Experiment of Influence of Distributed Roughness Elements on Hypersonic Boundary Layer Instability. *Acta Aeronaut. Astronaut. Sin.* **2024**, *45*, 128627.
15. Estorf, M.; Radespiel, R.; Schneider, S.; Johnson, H.; Hein, S. Surface-Pressure Measurements of Second-Mode Instability in Quiet Hypersonic Flow. In Proceedings of the 46th AIAA Aerospace Sciences Meeting and Exhibit, Reno, NV, USA, 7–10 January 2008; American Institute of Aeronautics and Astronautics: Reston, VA, USA, 2008.
16. Fujii, K. Experiment of the Two-Dimensional Roughness Effect on Hypersonic Boundary-Layer Transition. *J. Spacecr. Rocket.* **2006**, *43*, 731–738. [CrossRef]

17. Casper, K.M.; Beresh, S.J.; Schneider, S.P. Pressure Fluctuations beneath Instability Wavepackets and Turbulent Spots in a Hypersonic Boundary Layer. *J. Fluid Mech.* **2014**, *756*, 1058–1091. [CrossRef]
18. Luersen, R.P.K. Techniques for Application of Roughness for Manipulation of Second-Mode Waves on a Flared Cone at Mach 6. Master's Thesis, Purdue University, West Lafayette, IN, USA, 2012.
19. Houwing, A.F.P.; Smith, D.R.; Fox, J.S.; Danehy, P.M.; Mudford, N.R. Laminar Boundary Layer Separation at a Fin-Body Junction in a Hypersonic Flow. *Shock Waves* **2001**, *11*, 31–42. [CrossRef]
20. Mullen, C.D.; Turbeville, F.D.; Reed, H.L.; Schneider, S.P. Computational and Experimental Boundary-Layer Stability Analysis on a Hypersonic Finned Cone. In Proceedings of the AIAA SciTech 2019 Forum, San Diego, CA, USA, 7–11 January 2019; American Institute of Aeronautics and Astronautics: Reston, VA, USA, 2019.
21. Juliano, T.J.; Borg, M.P.; Schneider, S.P. Quiet Tunnel Measurements of HIFiRE-5 Boundary-Layer Transition. *AIAA J.* **2015**, *53*, 832–846. [CrossRef]
22. Borg, M.P.; Kimmel, R.L. Simultaneous Infrared and Pressure Measurements of Crossflow Instability Modes for HIFiRE-5. In Proceedings of the 54th AIAA Aerospace Sciences Meeting, San Diego, CA, USA, 4–8 January 2016; American Institute of Aeronautics and Astronautics: Reston, VA, USA, 2016.
23. Huang, R.; Cheng, J.; Chen, J.; Yuan, X.; Wu, J. Experimental Study of Bluntness Effects on Hypersonic Boundary-Layer Transition over a Slender Cone Using Surface Mounted Pressure Sensors. *Adv. Aerodyn.* **2022**, *4*, 35. [CrossRef]
24. Middlebrooks, J.B.; Corke, T.C.; Matlis, E.; Semper, M. Cross-Flow Instability on a Swept-Fin Cone at Mach 6: Characteristics and Control. *J. Fluid Mech.* **2024**, *981*, A18. [CrossRef]
25. Paredes, P.; Choudhari, M.M.; Li, F.; Jewell, J.S.; Kimmel, R.L.; Marineau, E.C.; Grossir, G. Nose-Tip Bluntness Effects on Transition at Hypersonic Speeds. *J. Spacecr. Rocket.* **2019**, *56*, 369–387. [CrossRef]
26. Hartman, A.B.; Hader, C.; Fasel, H.F. Nonlinear Transition Mechanism on a Blunt Cone at Mach 6: Oblique Breakdown. *J. Fluid Mech.* **2021**, *915*, R2. [CrossRef]

Disclaimer/Publisher's Note: The statements, opinions and data contained in all publications are solely those of the individual author(s) and contributor(s) and not of MDPI and/or the editor(s). MDPI and/or the editor(s) disclaim responsibility for any injury to people or property resulting from any ideas, methods, instructions or products referred to in the content.